Aerospace Science and Technology 180 (2027) 113614

Contents lists available at ScienceDirect

Aerospace Science and Technology

journal homepage: www.elsevier.com/locate/aescte

Wind tunnel tests of a tilt-rotor tailsitter with coordinated rotor tilt and elevon deflection

Ziqing Ma [a,b,*], Ewoud J. J. Smeur [a], Guido C. H. E. de Croon [a]

[a] Faculty of Aerospace Engineering, TU Delft, Delft, The Netherlands
[b] Department of Mechanical Engineering, The University of Hong Kong, Hong Kong SAR, China

ARTICLE INFO

Communicated by Dr Qu Qiulin

Keywords:
VTOL Aircraft
Tailsitter
Wind tunnel test
Wing-propeller interaction

ABSTRACT

This study investigates how coordinated rotor tilt and elevon deflection shape the aerodynamic performance and maneuvering capability of a tilt-rotor tailsitter UAV, with particular emphasis on high-speed sharp turns where maximizing lift is essential for minimizing turning radius. Extensive wind tunnel experiments were conducted across a range of airspeeds, angles of attack, throttle settings, and actuator combinations to quantify axial force, lift, and pitching moment while capturing the effects of wing–propeller interaction. Pitching-moment trim tests were also performed by dynamically adjusting actuator input combinations to maintain pitch moment equilibrium. The results show that upward rotor tilt, when combined with downward elevon deflection, produces substantially higher lift while preserving pitch moment equilibrium within the tested positive-AoA forward flight envelope, outperforming either actuation used alone. By embedding the derived empirical models into an equilibrium-constrained sharp turn maneuver, the study further predicts a theoretical minimum turning radius of 8.01 m at 18 m/s under an extrapolated throttle command condition, corresponding to a 31.8% reduction compared to an equivalent fixed-rotor tailsitter with elevons, suggesting that synergistic thrust vectoring and control-surface deflection enable aggressive maneuvers without compromising pitch stability or forward speed.

1. Introduction

Hybrid vertical take-off and landing (VTOL) aircraft integrate the efficient cruise performance of fixed-wing aircraft with the hovering and vertical lift capabilities of rotorcraft, making them well suited for missions such as aerial mapping, environmental monitoring, and search-and-rescue. Among the various hybrid VTOL designs, tailsitters are notable for their mechanically simple transition method, taking off and landing vertically on their tail and rotating their entire body to transition between hover and forward flight. Tailsitters can be classified into three main types based on their actuation control strategies. Traditional tailsitters are equipped with aerodynamic surfaces such as elevons [1], [2], [3], [4] (E-tailsitter), providing effective control at high speed but suffering from reduced pitch control authority and actuator saturation during low-speed flight. The tailsitter employing only thrust vectoring via tilting rotors [5] (TR-tailsitter) ensures reliable pitch control in vertical flight but lacks sufficient roll control during forward flight due to wing-propeller interaction. The TRE-tailsitter [6] combines both configurations by integrating tilting rotors with control surfaces, offering strong low-speed pitch control through thrust vectoring while retaining reliable roll control at high speeds. This integrated actuation scheme improves control effectiveness throughout the flight envelope and mitigates issues related to actuator saturation.

The ability to execute aggressive maneuvers is increasingly sought-after as tailsitters move from basic feasibility toward high-performance applications. Executing agile flight, including rapid accelerations, steep dives, or sharp turns, demands not only sufficient control authority but also effective coordination of the distinct actuator configurations inherent to tailsitters. Accurately predicting and controlling the aerodynamic forces in such conditions is therefore critical. A key factor complicating the guidance and modeling of aggressive turns for a tilt-rotor tailsitter is the strong aerodynamic coupling between the propellers, control surfaces, and the wing. The elevon deflection changes the wing's effective camber, and thrust vectoring modifies the local angle of attack (AoA); the combined effect of these actuators introduces complex aerodynamic interactions that significantly affect the forces and moments acting on the tilt-rotor tailsitter.

Some prior studies have investigated the isolated effects of control surface deflection or thrust vectoring on aerodynamic loads. On the one hand, deflection of control surfaces directly modifies the effective camber of the tailsitter wing and therefore influences both lift generation and pitching moment [7], [8]. According to [9], propeller slipstream

* Corresponding author.
E-mail addresses: Z.Ma@tudelft.nl (Z. Ma), E.J.J.Smeur@tudelft.nl (E.J.J. Smeur), G.C.H.E.deCroon@tudelft.nl (G.C.H.E. de Croon).

https://doi.org/10.1016/j.ast.2026.113614
Received 31 December 2025; Received in revised form 5 July 2026; Accepted 21 August 2026
Available online 26 August 2026

can significantly modify the lift distribution over wings equipped with trailing-edge flaps, with the resulting lift changes depending on the flap deflection and local flow conditions. An integrated panel and blade-element method is developed in [10] to model a tailsitter UAV, revealing that the control surfaces of a tailsitter are typically submerged in the propeller slipstream, where the enhanced local flow velocity dominates the aerodynamic loads and control authority, especially during low-speed flight. On the other hand, thrust vectoring through rotor tilt alters the local angle of attack over the wing in a more complex manner. In [11], thrust vectoring in tilt-rotor configurations introduces strong rotor–wing aerodynamic interactions, significantly affecting lift distribution and pitching moments across hover, conversion, and cruise flight regimes. Numerical investigations of a tilt-rotor aircraft as described in [12] further reveal that rotor orientation and induced flow strongly influence wing aerodynamics and aerodynamic load distribution through rotor–wing–fuselage interaction. The impact of propeller position and AoA on lift and drag is quantified in [13], highlighting that in tilt-rotor configurations, reduced propeller–wing spacing can substantially increase wing lift while decreasing drag. It is illustrated in [14] that for distributed propulsion with thrust vectoring, deflected propulsive jets alter the lift curve slope, maximum lift, and pitching moment of the airfoil, highlighting the aerodynamic coupling between thrust vectoring and lifting surfaces.

In spite of the contributions made by previous research, the combined aerodynamic effects resulting from both rotor tilt and elevon deflection in a tilt-rotor tailsitter configuration remain insufficiently characterized, especially during aggressive maneuvers such as sharp turns that involve coordinated actuator inputs. Prior studies on propeller-slipstream effects have shown that the aerodynamic loads and control authority of downstream control surfaces can be strongly affected by the local induced flow, but these studies primarily consider configurations in which the propeller orientation is fixed and is not varied as an additional control input. Conversely, studies on tiltrotor aerodynamics and thrust-vectoring propulsion have mainly examined how rotor orientation and induced flow modify the aerodynamic loading of lifting surfaces, without simultaneously varying a downstream control surface such as an elevon. Therefore, the key unresolved problem is not the existence of propeller-wing interaction or control-surface effectiveness individually, but the coupled aerodynamic response that arises when rotor tilt angle and elevon deflection are varied concurrently on the same tailsitter vehicle. This coupling is especially important for high-speed turning scenarios, where upward rotor tilt can increase the vertical thrust component and modify the local inflow over the wing, while downward elevon deflection can increase lift and provide the opposing pitching moment required for trim. A thorough analysis of the coupled rotor-wing-elevon interaction is therefore essential for identifying actuator combinations that can simultaneously generate high lift and maintain pitch moment equilibrium.

Motivated by the potential and unresolved challenges of achieving sharp turns with a tilt-rotor tailsitter, this work presents a dedicated experimental investigation of a tailsitter's aerodynamics under conditions representative of sharp-turn maneuvers. A comprehensive wind tunnel campaign was carried out with the test tilt-rotor tailsitter rigidly mounted on a six-axis force/moment sensor to measure the forces and moments acting on the vehicle across a range of variations in rotor tilt angle, elevon deflection, thrust level, angle of attack and airspeed. In contrast to prior tailsitter studies that primarily considered either elevon effects under a fixed rotor orientation or rotor-tilt effects without simultaneous elevon variation, the present experiments vary rotor tilt angle and elevon deflection concurrently on the same tilt-rotor tailsitter. This allows the coupled aerodynamic response associated with changes in rotor orientation, propeller-induced local inflow over the wing and elevon, wing loading, and elevon-generated pitching moment to be characterized in an integrated manner. To the best of our knowledge, this work provides the first empirical dataset [15] and model for a tilt-rotor tailsitter UAV that systematically captures the coupled aerodynamic response under combined variations of rotor tilt angle and elevon deflection, across different angles of attack and airspeeds. Through the pitching moment trim experiments, the study identifies that actuator combinations of upward rotor tilt and downward elevon deflection enable the vehicle to simultaneously generate high lift and maintain pitch moment equilibrium within the tested positive-AoA forward flight envelope, which serves as a proxy for the vehicle's capability to perform sharp coordinated turns. Furthermore, using the derived empirical aerodynamic model, the study evaluates the potential sharp-turn performance of the proposed tilt-rotor tailsitter at a given flight speed of 18 m/s. Under the extended throttle-command range, the equilibrium analysis predicts a theoretical minimum turning radius of 8.01 m, corresponding to a 31.8% reduction relative to an equivalent fixed-rotor elevon-only baseline under the same analysis assumptions. This result is therefore used as an extrapolated performance bound predicted by the wind-tunnel-derived empirical model, rather than as a fully experimentally validated flight performance prediction. Overall, this work demonstrates that in the tested positive-AoA forward-flight wind tunnel envelope, coordinated thrust vectoring and elevon deflection can expand the maneuvering capability of hybrid aircraft by increasing lift without sacrificing pitch trim or forward-speed sustainability, thereby providing a promising performance benchmark for agile maneuvering with hybrid aircraft.

The remainder of this paper is structured as follows. Section 2 introduces the experimental setup, including the tilt-rotor tailsitter model, instrumentation, and wind tunnel configuration. Section 3 presents the static wind tunnel tests that examine the aerodynamic response under varying rotor tilt and elevon inputs and develops an empirical model using multivariate regression. Section 4 details the pitch moment trimming wind tunnel experiments with real-time actuator control to achieve pitch moment equilibrium, and extends the analysis using the empirical model to map lift force contours overlaid with zero pitch moment lines under combined actuation inputs. Section 5 explores optimal actuation strategies for theoretical minimum turning radius in high-speed turning scenarios. Finally, Section 6 concludes this paper and discusses the future work for achieving agile sharp turns with tilt-rotor tailsitter UAVs.

2. Wind tunnel experiment design

2.1. Experiment proposal

Tilt-rotor tailsitters offer a unique actuator redundancy by combining rotor thrust vectoring with aerodynamic surface control. From fundamental aerodynamic principles, an upward rotor tilt produces additional vertical force, reduced local angle of attack and a pitch-up moment, while a downward deflected elevon increases lift and induces a pitch-down moment. Inspired by this complementary effect, we hypothesize that a coordinated combination of upward tilt and downward elevon deflection can achieve increased lift while maintaining pitch moment equilibrium, which is especially a critical condition for sharp coordinated turns. Fig. 1 schematically illustrates the concept.

However, the presence of wing–propeller interaction, especially the propeller-induced flow over the wing, introduces nonlinear aerodynamic coupling that challenges intuitive predictions. To rigorously investigate the aerodynamic effects of actuator combinations and to evaluate the proposed hypothesis, we design a series of wind tunnel experiments targeting force and moment characterization. The first measurement series consist of static measurement tests, in which forces and moments are recorded under systematically varied actuator configurations across different angles of attack and freestream airspeeds, aimed at developing experimental numerical models. The second type is pitching moment trimming tests, in which the elevon deflection is dynamically adjusted in real time to balance the pitch moment induced by rotor tilt, thereby evaluating the feasibility of achieving moment equilibrium under actuator coordination.

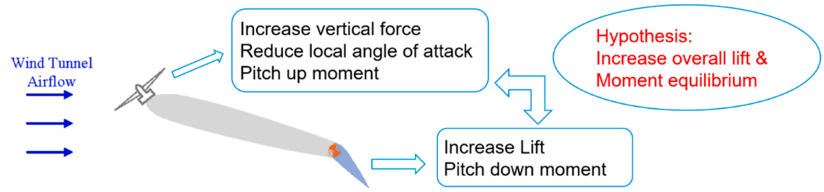

Fig. 1. Schematic concept of combined tilt and elevon deflection for enhanced lift generation while maintaining pitch moment equilibrium.

Fig. 2. Wind tunnel experimental setup pictures showing the tilt-rotor tailsitter mounted on a six-axis force/torque sensor in the OJF wind tunnel [16], with a servo-driven mechanism to adjust angle of attack.

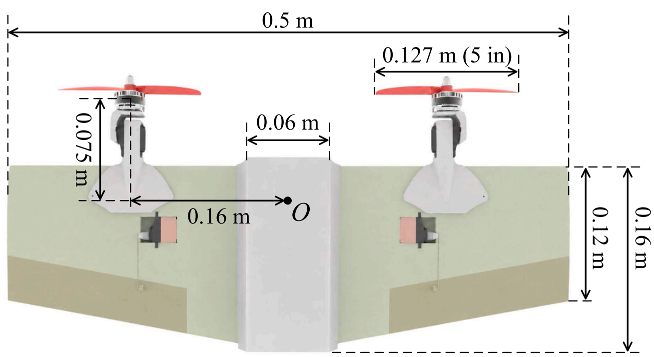

Fig. 3. Schematic figure of the tested tilt-rotor tailsitter platform from the bird's eye view.

2.2. Experiment setup

To analyze aerodynamic characterization of wing-propeller interaction in a tilt-rotor tailsitter for sharp turn maneuvers, a series of wind tunnel tests were conducted to investigate the aerodynamic behavior of a custom-built tilt-rotor tailsitter in the Open Jet Facility (OJF) low-speed wind tunnel, whose test section outlet measures 2.85 m in both width and height. The test platform is a custom-built tilt-rotor tailsitter, featuring a pair of rotors with variable tilt in the pitch plane and a set of trailing-edge elevons. The airframe has a wingspan of 0.5 m and uses a symmetric NACA0012 airfoil profile.

As Fig. 2 displays, the tilt-rotor tailsitter, whose specific geometry is displayed in Fig. 3, is mounted in a horizontal, forward-flight configuration within the wind tunnel test section, with its longitudinal axis aligned with the freestream flow. The propulsive system of the tested drone consists of EMAX ECO II 2207–2400KV brushless motors, Eachine 5045 propellers, and DYS AM32 70A electronic speed controllers. The support assembly consists of multiple modular components to ensure accurate load measurement and precise control of the angle of attack. Structurally, the drone airframe is attached to a 3D-printed mounting interface, which is connected to a six-axis force/torque sensor (ATI Mini45, IP65-rated) by a support bar. The force/torque sensor used in this study has measurement ranges of ±145 N for F_x and F_y, ±290 N for F_z, and ±5 N m for T_x, T_y, and T_z. The corresponding rated resolutions are 1/16 N for the force channels, 1/752 N m for T_x and T_y, and 1/1504 N m for T_z. An additional custom-printed connector links the sensor to a Xiaomi CyberGear servo, which enables automated control of the drone's angle of attack by rotating the entire upper assembly as a single rigid body about the pitch axis. All modular components remained mechanically fixed relative to each other during testing, ensuring aerodynamic loads to be transmitted directly and without distortion to the force/torque sensor for accurate measurements. With the instrumentation described, force and moment data were successfully captured in real time, enabling both static measurements and pitching moment trim tests. In the present experimental setup, several assumptions are made. First, at large angles of attack, the wake generated by the servo and mounting components may interact with the flow around the airframe. However, this effect is assumed to be small and is not explicitly corrected for. Second, tilting the rotors and, to a lesser extent, deflecting the elevons slightly shifts the vehicle's center of gravity. This shift may affect the measured pitching moment by changing the effective moment arms of the thrust and aerodynamic forces relative to the assumed reference point. However, because the moving components are small compared with the total vehicle mass and their displacement is limited by the actuator range, the resulting CG shift is expected to be small relative to the measured aerodynamic and propulsive pitching moments. Therefore, this effect is not explicitly corrected in the force and moment processing, but is acknowledged as a potential source of measurement uncertainty.

To quantify the aerodynamic forces and pitching moment acting on the tilt-rotor tailsitter, we define three right-handed coordinate frames: the measurement frame (x_m, y_m, z_m) fixed to the ATI force/torque sensor, the body frame (x_B, y_B, z_B) fixed to the drone, and the freestream aligned aerodynamic frame(x_A, y_A, z_A), with axis positive directions defined in Fig. 4. The sensor measurement frame follows the right-hand rule. Due to the mechanical installation of the force/torque sensor, a

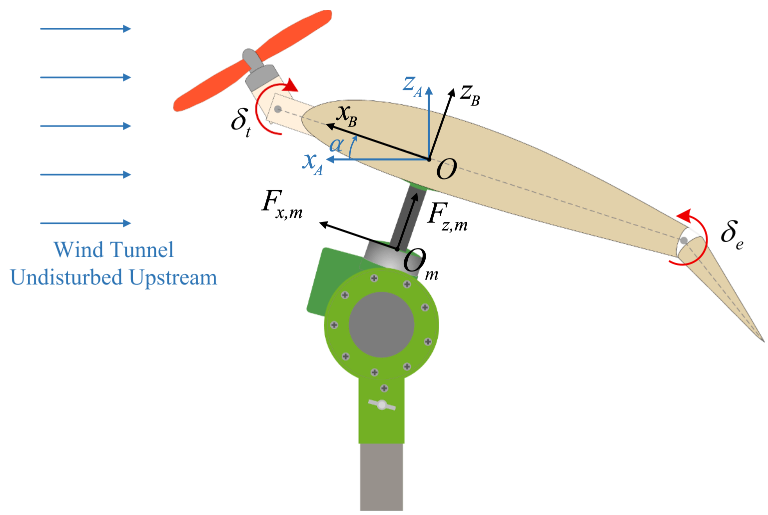

Fig. 4. Wind tunnel experimental setup schematic figure showing the tilt-rotor tailsitter mounted on a six-axis force/torque sensor in the OJF wind tunnel, with a servo-driven mechanism to adjust angle of attack and red arrows suggesting the positive direction for rotor tilt and elevon deflection. (For interpretation of the references to colour in this figure legend, the reader is referred to the web version of this article.)

positive measured moment $M_{y,m}$ corresponds to a pitch-down rotation of the aircraft, which is opposite to the conventional aerospace sign convention. For the sake of consistency between the measurement frame and the body frame, the body axes (x_b, y_b, z_b) are defined to be aligned with the sensor axes (x_m, y_m, z_m). All forces and moments reported in this paper strictly follow this coordinate definition. The reference point of forces and moment is defined at the drone's center of gravity, located 0.03 m from the leading edge.

To extract the net aerodynamic forces and pitching moment, including the effects of rotor thrust and aerodynamic loads, we remove the baseline gravitational contributions measured under no-wind conditions and measurements under wind for the bar that connects the drone and the sensor. The detailed calculation is shown as follows:

$$F_{x,B} = F_{x,m} - F_{x,m}^{(\mathrm{bw})} - \left(F_{x,m}^{(\mathrm{dg})} - F_{x,m}^{(\mathrm{bg})}\right), \tag{1}$$

$$F_{z,B} = F_{z,m} - F_{z,m}^{(\mathrm{bw})} - \left(F_{z,m}^{(\mathrm{dg})} - F_{z,m}^{(\mathrm{bg})}\right), \tag{2}$$

$$F_{x,A} = F_{x,B}\cos\alpha - F_{z,B}\sin\alpha, \tag{3}$$

$$F_{z,A} = F_{x,B}\sin\alpha + F_{z,B}\cos\alpha, \tag{4}$$

$$M_{y,A} = M_{y,B} = M_{y,m} - M_{y,m}^{(\mathrm{bw})} - F_{x,m}^{(\mathrm{dg})} \cdot d_{CG}. \tag{5}$$

Specifically, $F_{x,m}$ and $F_{z,m}$ denote the forces measured for the complete setup, the support bar and drone, under wind tunnel freestream conditions. The quantities $F_{x,m}^{(\mathrm{bw})}$ and $F_{z,m}^{(\mathrm{bw})}$ are measured for the bar alone under the same airspeed condition, which include both the aerodynamic loads on the bar and its gravitational components. In addition, $F_{x,m}^{(\mathrm{dg})}$ and $F_{z,m}^{(\mathrm{dg})}$ are obtained for the full setup with the wind tunnel powered off, which represent the combined gravitational forces of the bar and the drone. Finally, $F_{x,m}^{(\mathrm{bg})}$ and $F_{z,m}^{(\mathrm{bg})}$ are measured for the bar alone without wind tunnel freestream, corresponding to the bar's gravitational contribution. Therefore, the subtraction $F_{x,m} - F_{x,m}^{(\mathrm{bw})}$ removes the aerodynamic and gravitational effects of the bar from the total measurement, yielding the combined effect of the drone's aerodynamics, thrust and gravity. The subsequent term $F_{x,m}^{(\mathrm{dg})} - F_{x,m}^{(\mathrm{bg})}$ isolates the gravitational force acting on the drone. Subtracting this gravity term finally yields the resultant force acting on the drone excluding gravity, including both thrust and aerodynamic contributions, as shown in Eq. (1) and similarly for the z-axis. This procedure accounts for changes in the gravitational force components caused by variation of the angle of attack during the tests and ensures that only non-gravitational force contributions are retained. $M_{y,m}$ is the pitching moment measured by the sensor; $M_{y,m}^{(\mathrm{bw})}$ denotes the bar-alone pitch moment measured under freestream conditions. Since the gravitational force acts through the drone's center of gravity, it does not generate a pitching moment about the y-axis in the body-fixed frame. Consequently, no additional gravity-related correction is required for the pitching moment. Here, α denotes the angle of attack, and $d_{CG} = 0.95$ m is the distance from the sensor measurement plane to the drone's center of gravity.

It should be noted that the force/torque sensor was not enclosed by an aerodynamic fairing. Aerodynamic tare measurements of the support bar and sensor assembly were conducted and subtracted from the total measurements under the same freestream conditions, as described above. This procedure removes the freestream-induced loads on the supporting bar and the sensor assembly. However, it does not fully account for possible interaction effects between the propeller wake and the measurement balance, particularly at large rotor tilt angles. Although these effects are expected to be secondary to the vehicle loads, they are acknowledged as a potential source of uncertainty in the reported force and moment data.

3. Static measurement test

3.1. Static test matrix

The static wind tunnel experiments primarily aim to characterize the aerodynamic behavior of the tilt-rotor tailsitter under a representative range of flight and actuation conditions, with a particular focus on the influence of coupled actuator inputs on lift and pitching moment generation. The experimental campaign systematically explores how these aerodynamic forces and moments vary with key parameters including angle of attack (α), airspeed (V), motor throttle setting (T), elevon deflection (δ_e), rotor tilt angle (δ_t) and their coupling terms. Specifically, the motor throttle setting represents the PWM command percentage normalized with respect to the full PWM range, rather than a closed-loop RPM-control mode. Since no direct RPM, thrust, or torque measurements are available, the throttle setting is used here as a control input variable rather than as a direct physical parameter. This parameter space is designed to capture the interaction between wing aerodynamics and rotor-induced flow, which plays a critical role in maneuvering performance and control authority.

Wind tunnel airspeeds of 15 and 18 m/s were selected as representative forward flight velocities for evaluating maximum lift capability and maneuvering performance. These values enable estimation of the maximum lift and corresponding minimum turning radius under realistic operating conditions. These discrete setpoints balance coverage of relevant dynamic pressure regimes with practical limitations on test duration. At each airspeed, the tilt-rotor tailsitter was tested across the range of 0° up to 20° with a 5° interval. This AoA range captures typical flight attitudes from level cruise to moderate pitching up, representative of initiating a high-g turn, but avoids deep stall or post-stall angles that are outside the scope of high-speed maneuvers. For each flight condition, the drone was subjected to various combinations of actuator configurations, specifically, 0, 30%, 40% and 45% for throttle level, 0, ±15.8°, ±31.5°, ±47.3°, ±63° for elevon deflection and 0, 15.8°, 31.5°, 47.3° for rotor tilt). Each configuration lasted for 8 seconds and the mean force and moment values were recorded for further analysis. To provide a reference physical interpretation of the open-loop throttle commands, additional no-wind RPM measurements were conducted using the same motor–propeller–ESC configuration. The measured no-wind rotational speeds corresponding to the 30%, 40%, and 45% throttle commands were 9600, 13629, and 15257 rpm, respectively.

3.2. Direct aerodynamic trends from measured data

Before introducing the empirical regression model, selected wind tunnel measurements are examined directly to identify the main aerodynamic trends associated with elevon deflection and rotor tilt. This analysis is intended to provide physical interpretation of the measured data independently of the subsequent fitting procedure. The force and moment data are converted into the overall lift coefficient $C_{Z,A}$, net axial-force coefficient $C_{X,A}$, and pitching-moment coefficient C_m. Here, $C_{X,A}$ and $C_{Z,A}$ represent both aerodynamic and propulsive contributions, rather than a pure aerodynamic lift or drag coefficient. It should also be noted that, due to the sensor mounting orientation, negative M_y corresponds to a pitch-up moment in the body-fixed frame. The coefficients are evaluated at discrete angles of attack under a fixed airspeed of $V = 18$ m/s and throttle setting of $T = 40\%$.

The measured trends in Fig. 5 reveal several coupled effects that are specific to the tested tilt-rotor tailsitter configuration. For the fixed positive rotor-tilt case shown in the left column, increasing upward elevon deflection has only a limited additional influence on $C_{X,A}$ as the angle of attack increases. In contrast, downward elevon deflection consistently drives $C_{X,A}$ toward more negative values over the tested angle-of-attack range, indicating a stronger axial-force penalty associated with lift enhancement from the control surface. The corresponding $C_{Z,A}$ trends show that downward elevon deflection always produces higher lift than upward deflection. However, the lift increment produced by the elevon gradually decreases at higher angles of attack, and the separation between positive and negative elevon deflections becomes smaller. This suggests that the elevon effectiveness in lift generation is reduced as the wing angle of attack increases, likely due to stronger nonlinear flow effects near the deflected control surface. The pitching-moment trends further show that, under positive rotor tilt, downward elevon deflection can increase $C_{Z,A}$ while keeping C_m close to zero over part of the tested envelope, which is favorable for pitch-moment equilibrium. The right column provides the complementary effect of rotor tilt under a fixed downward elevon deflection. Increasing rotor tilt raises $C_{Z,A}$, as expected from the vertical component of the tilted thrust vector, but its incremental effect on lift is smaller than the change produced by elevon deflection of comparable angular magnitude. Notably, the influence of rotor tilt on $C_{X,A}$ becomes moderately evident at larger angles of attack, indicating that when the vehicle operates with a downward elevon and high angle of attack, the reduction of axial thrust projection and the increase in aerodynamic drag become more pronounced as the rotor is tilted upward. A comparison between the two yellow curves further highlights the different roles of the two actuators. The case with $\delta_t = 0°$ and $\delta_e = -31.5°$ produces a larger lift coefficient and a more negative axial-force coefficient than the case with $\delta_t = 31.5°$ and $\delta_e = 0°$. Thus, for comparable actuator angular deflections, the elevon has a stronger effect on both lift generation and axial-force penalty, whereas rotor tilt provides a more moderate lift increase through thrust-vector reorientation.

Table 1
Summary of input variables, physical operating envelopes, and normalization scaling ranges used in the regression analysis.

Variable	Unit	Physical Range	Normalized Range	Scaling Type
δ_t	deg	$[0, 47.3]$	$[0, 1]$	Min-Max
α	deg	$[0, 20]$	$[0, 1]$	Min-Max
δ_e	deg	$[-63, 63]$	$[-1, 1]$	Center-Scale
V	m/s	$[0, 20]$	$[0, 1]$	Min-Max
T	-	$[0, 1]$	$[0, 1]$	Identity

These observations show that lift generation, axial-force balance, and pitching moment are coupled through both actuator inputs and flight condition, motivating the empirical modeling approach developed in the following section to quantify these effects over the tested parameter space.

3.3. Empirical modeling of aerodynamic forces and moments

To quantitatively describe the aerodynamic behavior of the tailsitter, empirical regression models are constructed to represent the overall lift, net axial force, and pitching moment as functions of rotor tilt angle (δ_t), motor throttle setting (T), elevon deflection (δ_e), angle of attack (α), and airspeed (V). All input variables are normalized using a range-based scaling approach defined on their physical operating envelopes. Specifically, each variable is linearly mapped from a representative physical range to a dimensionless interval of either $[0, 1]$ or $[-1, 1]$, as summarized in Table 1, such that the regression coefficients remain directly comparable across variables in terms of relative magnitude. Trigonometric terms are included to account for the nonlinear thrust vectoring introduced by tilt rotors, and a cubic term in elevon deflection is incorporated to capture the nonlinear degradation of control effectiveness at large deflections as described in [17].

By sweeping these parameters individually and in combination, the resulting empirical models incorporate linear, quadratic, and interaction terms, yielding a total of 35 candidate features in the initial regression pool. An initial feature selection is performed using the Least Absolute Shrinkage and Selection Operator (LASSO) regression [18], promoting sparsity while retaining predictive power. This reduces the candidate set to 24, 25, and 19 features for lift, pitching moment, and axial force, respectively, by eliminating irrelevant or redundant terms. The retained features are subsequently evaluated using a forward stepwise selection, as illustrated in Fig. 6. At each step, the feature that yields the largest reduction in mean squared error (MSE) is added to the model, producing an ordered ranking of explanatory importance based on marginal contribution to model accuracy. A cutoff criterion is then applied based on retaining 98% of the total achievable MSE reduction, defined as the difference between the intercept-only model and the model including all preselected features. Consequently, 12, 10, and 11 terms (including an intercept) are retained for $F_{X,A}$, M_y, and $F_{Z,A}$, respectively, striking a balance between estimation fidelity and model simplicity.

Based on these selected terms, the final multivariate polynomial models describing axial force, pitching moment, and lift as functions of angle of attack, airspeed, throttle, rotor tilt, and elevon deflection are expressed as follows. For clarity, all variables appearing in Eqs. (6)–(8) refer to the normalized variables defined in Table 1, unless stated otherwise.

$$\begin{aligned}F_{X,A}(\alpha, V, T, \delta_e, \delta_t) = {} & C_{x0} + C_{x\alpha}\,\alpha + C_{x\alpha^2}\,\alpha^2 + C_{xV^2}\,V^2 \\ & + C_{xT^2}\,T^2 + C_{x\delta_e^2}\,\delta_e^2 \\ & + C_{x\delta_e\alpha}\,\delta_e\alpha + C_{x\delta_e^3}\,\delta_e^3 + C_{x\alpha\delta_e^3}\,\alpha\,\delta_e^3 + C_{x\delta_e^4}\,\delta_e^4 \\ & + C_{xT\cos\delta_t}\,T\cos\delta_t + C_{x\cos^2(\delta_t)}\cos^2(\delta_t)\end{aligned} \tag{6}$$

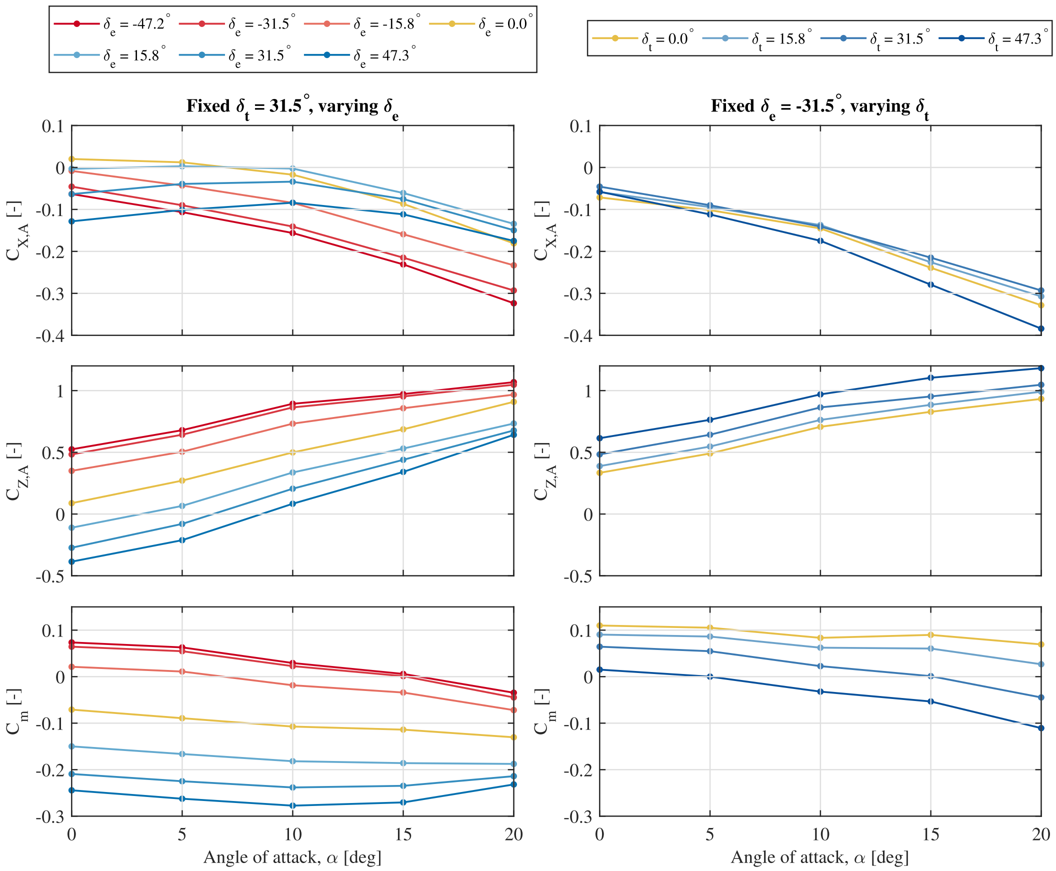

Fig. 5. Measured net axial-force coefficient $C_{X,A}$, lift coefficient $C_{Z,A}$, and pitching-moment coefficient C_m at discrete angles of attack under $V = 18$ m/s and $T = 40\%$. Markers denote wind-tunnel measurements, and connecting lines are included only to indicate trends. Left column: varying elevon deflection at fixed rotor tilt $\delta_t = 31.5°$. Right column: varying rotor tilt at fixed elevon deflection $\delta_e = -31.5°$.

$$\begin{aligned} M_y(\alpha, V, T, \delta_e, \delta_t) = {} & C_{m0} + C_{m\alpha}\,\alpha + C_{m\delta_e\alpha}\,\delta_e\alpha + C_{m\delta_t\delta_e}\,\delta_t\delta_e \\ & + C_{m\delta_e V^2}\,\delta_e V^2 + C_{m\delta_t T}\,\delta_t T \\ & + C_{mV^2\delta_e^3}\,V^2\delta_e^3 + C_{mT\delta_e}\,T\delta_e \\ & + C_{m\delta_t\alpha}\,\delta_t\alpha + C_{mT\alpha}\,T\alpha. \end{aligned} \tag{7}$$

$$\begin{aligned} F_{Z,A}(\alpha, V, T, \delta_e, \delta_t) = {} & C_{z0} + C_{z\delta_e V^2}\,\delta_e V^2 + C_{z\alpha V^2}\,\alpha V^2 + C_{z\delta_t T}\,\delta_t T \\ & + C_{z\alpha\delta_e^3}\,\alpha\delta_e^3 + C_{zT\delta_e}\,T\delta_e + C_{zV^2\delta_e^3}\,V^2\delta_e^3 \\ & + C_{zV^2}\,V^2 + C_{z\delta_e\alpha}\,\delta_e\alpha + C_{zT\alpha}\,T\alpha + C_{z\alpha^2}\,\alpha^2. \end{aligned} \tag{8}$$

The estimated coefficients of the scaled polynomial models are summarized in Table 2, providing a quantitative description of the static aerodynamic behavior of the tilt-rotor tailsitter under coupled variations of flight conditions and control inputs. The resulting models demonstrate high predictive accuracy, with coefficients of determination of 0.915, 0.963, and 0.972 for axial force, pitching moment, and lift, respectively. The corresponding root mean square errors are 0.458 N for $F_{X,A}$, 0.042 N·m for M_y, and 0.604 N for $F_{Z,A}$. To indicate the relative magnitude of the force-fitting errors, the force RMSE values are additionally normalized by the vehicle weight, resulting in 9.4% for $F_{X,A}$ and 12.3% for $F_{Z,A}$. These values indicate that the fitting uncertainty is not negligible on the vehicle-weight scale, especially for the lift model. However, the same RMSE values correspond to 6.1% of the measured $F_{X,A}$ range and 2.4% of the measured $F_{Z,A}$ range, respectively. The moment RMSE is retained in dimensional form because its normalized value depends on the choice of a reference moment. Together with the high coefficients of determination, these results indicate that the polynomial models capture the dominant force and moment trends over the tested envelope and can be used as empirical interpolation models to support

Table 2
Regression coefficients of the normalized polynomial models for axial force $F_{X,A}$, pitching moment M_y, and lift $F_{Z,A}$.

Feature	Coef. ($F_{X,A}$)	Coef. (M_y)	Coef. ($F_{Z,A}$)
Intercept	2.6987	−0.0058	2.8861
α	−1.1582	−0.00545	—
α^2	−1.5623	—	−2.3414
$\delta_e\alpha$	2.6779	0.0819	3.6395
$\alpha\delta_e^3$	−1.1351	—	−1.1517
δ_e^4	1.7069	—	—
V^2	−4.8821	—	−3.9620
$\delta_e V^2$	—	−0.5346	−12.4090
αV^2	—	—	14.6860
δ_e^2	−2.8649	—	—
δ_e^3	−0.5078	—	—
$V^2\delta_e^3$	—	0.2950	5.8411
T^2	4.1031	—	—
$T\delta_e$	—	−0.2427	−3.8545
$T\alpha$	—	−0.1070	3.2568
$\delta_t T$	—	−0.6293	4.9680
$\delta_t\delta_e$	—	−0.0580	—
$\delta_t\alpha$	—	−0.0664	—
$T\cos\delta_t$	1.9693	—	—
$\cos^2\delta_t$	−0.3291	—	—
Model R^2	0.915	0.963	0.972
RMSE	0.458 N	0.042 N·m	0.604 N

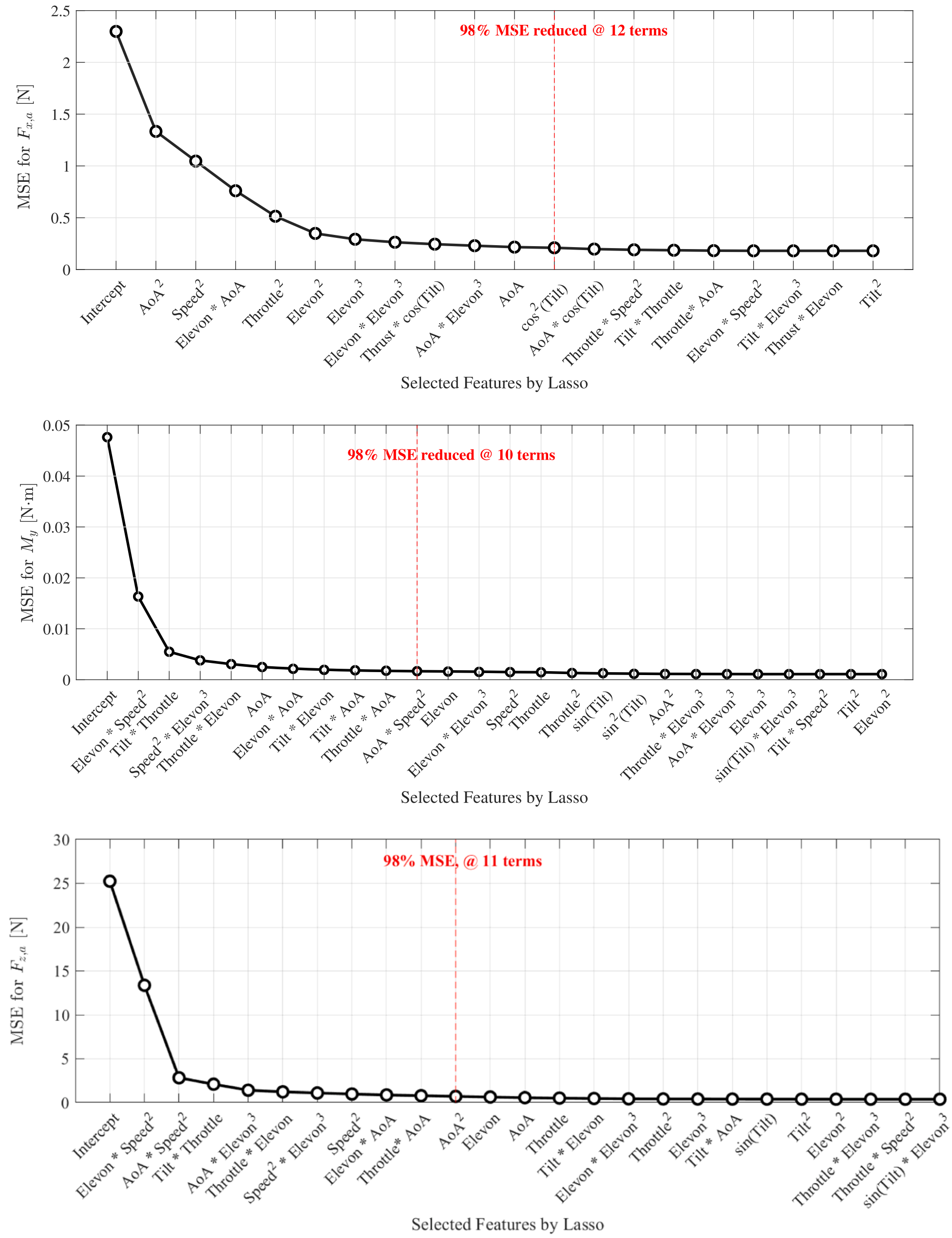

Fig. 6. Mean squared error (MSE) convergence curves from build-up regression based on LASSO-selected features for $F_{Z,A}$, M_y and $F_{X,A}$. Features are incrementally added in order of their individual R^2 values. The red dashed line indicates the point where 98% of total MSE reduction is achieved. (For interpretation of the references to colour in this figure legend, the reader is referred to the web version of this article.)

trend analysis, feasible operating-region search, and interpretation of actuator effects. The identified terms reveal dominant aerodynamic trends as well as nonlinear cross-coupling effects between airspeed, rotor tilt, throttle, and elevon deflection. Quantitative predictions from the fitted models should therefore be interpreted within the tested wind-tunnel envelope, while the observed aerodynamic trends and the coordinated-actuation principle provide useful physical insight for similar tilt-rotor tailsitter configurations.

For the axial-force $F_{X,A}$ model, both α and V^2 exhibit negative main effects, reflecting the increase of axial drag with larger angle of attack and airspeed. The negative quadratic term $C_{x\alpha^2}\,\alpha^2$ captures the quadratic rise in induced drag and the onset of flow separation in the post-linear regime. It should be noted that $F_{X,A}$ is the net axial-force component expressed in the freestream-aligned aerodynamic frame, rather than an isolated aerodynamic load of the airframe. The α-dependent terms should not be interpreted as a freestream drag contribution at $V = 0$. The wind-off measurements are used for baseline and gravity correction, and the model is intended for interpolation within the tested forward-flight conditions. The αV^2 term was included in the candidate set, but was not retained by the sparse identification procedure, indicating that it was not independently dominant over the tested envelope. This does not exclude physical angle-of-attack and dynamic-pressure coupling, as shown by the retained αV^2 term in the $F_{Z,A}$ model. The throttle contribution is dominated by a strong positive quadratic term $C_{xT^2}\,T^2$, implying that thrust increases nonlinearly with throttle command in the axial direction, outweighing aerodynamic drag at higher throttle settings. With respect to elevon deflection, the dominant negative quadratic term $C_{x\delta_e^2}\,\delta_e^2$ captures the fundamental rise in profile drag with deflection. Notably, the positive fourth-order term $C_{x\delta_e^4}\,\delta_e^4$ acts as an empirical saturation correction at large deflections. This term should not be interpreted as a standalone first-principles aerodynamic mechanism, but rather as a compact correction that captures the nonlinear variation of elevon-induced axial force within the tested envelope. Furthermore, the interaction term $C_{x\delta_e\alpha}\,\delta_e\alpha$ carries a positive coefficient, which suggests that deflecting the elevon upward at high angles of attack helps align the trailing edge with the local flow, thereby alleviating the drag penalty. Finally, the tilt effect enters the model primarily through the term $C_{xT\cos\delta_t}\,T\cos\delta_t$ with a strong positive coefficient, demonstrating that the axial force is governed by the geometric cosine projection of the rotor thrust vector.

For the pitching-moment model M_y, both elevon deflection δ_e and rotor tilt δ_t play dominant roles, together with their coupling with airspeed and thrust. It should be noted that due to the sensor mounting orientation, negative M_y corresponds to a pitch up moment in the body frame. The aerodynamic control authority is captured primarily by the interaction term $C_{m\delta_e V^2}\,\delta_e V^2$ with a negative coefficient, confirming that control effectiveness scales with dynamic pressure. The nonlinear saturation of elevon control authority is modeled by the velocity-weighted cubic term $C_{mV^2\delta_e^3}\,V^2\delta_e^3$ (positive coefficient) in strongly deflected, high speed conditions. Furthermore, the significant term $C_{mT\delta_e}\,T\delta_e$ indicates that increasing throttle enhances the pitching moment generated by elevon deflection even at low airspeeds, consistent with the propeller slipstream energizing the flow over the control surface. The structure of the identified model provides compelling empirical support for the proposed trim strategy of utilizing downward elevon deflection to counteract the moment induced by upward rotor tilt. The dominant bilinear term $C_{m\delta_t T}\,\delta_t T$ exhibits a large negative coefficient, confirming that increasing throttle in a tilt-up configuration ($\delta_t > 0$) introduces a powerful pitch up moment via the inclined thrust vector. Maintaining equilibrium therefore requires a counter-acting positive (pitch down) moment. By applying a downward elevon deflection ($\delta_e < 0$), the primary control term $C_{m\delta_e V^2}\,\delta_e V^2$ yields a positive contribution, providing the necessary opposing pitch down moment to the thrust vector. Further interaction terms involving $C_{m\delta_t\delta_e}\,\delta_t\delta_e$ and $C_{m\delta_t\alpha}\,\delta_t\alpha$ with moderate coefficients indicate that rotor tilt modifies the local angle of attack and loading on the wing and elevon, so that the pitching moment is sensitive to the combined setting of rotor tilt, elevon deflection and angle of attack.

For the identified empirical model of $F_{Z,A}$, the lift is governed primarily by angle of attack α, elevon deflection δ_e, airspeed V, and thrust vectoring effects, reflecting the combined aerodynamic and propulsive nature of the tailsitter configuration. The dominant coefficients of the terms $C_{z\alpha V^2}\,\alpha V^2$ and $C_{z\delta_e V^2}\,\delta_e V^2$ confirm that the primary lift generation scales significantly with dynamic pressure. However, the quadratic term $C_{z\alpha^2}\,\alpha^2$ implies the onset of nonlinear lift degradation at higher angle of attack, reflecting the early stall characteristics and flow separation. The model also captures saturation effects through the velocity-weighted cubic term $C_{zV^2\delta_e^3}\,V^2\delta_e^3$ and the interaction term $C_{z\alpha\delta_e^3}\,\alpha\delta_e^3$, further suggesting that at higher angles of attack, excessive elevon deflection becomes less effective in augmenting lift, likely due to the combined effects of flow separation on the control surface and propeller slipstream distortion. Notably, rotor tilt affects the lift generation through two competing mechanisms. On one hand, tilting the rotor upward increases the vertical component of thrust, thereby directly contributing to lift via thrust vectoring. On the other hand, rotor tilt also alters the local inflow direction over the wing, reducing the local angle of attack and hence decreasing the aerodynamic lift component. The positive coefficient of the term $C_{z\delta_t T}\,\delta_t T$ confirms that the thrust induced vertical force outweighs the loss of wing lift caused by local angle of attack reduction under the tested conditions. This demonstrates that, for a tilt-rotor configuration, thrust vectoring plays a leading role in supporting lift, while the adverse aerodynamic effect associated with local angle of attack reduction remains secondary. Furthermore, the interaction term $C_{zT\alpha}\,T\alpha$ indicates that lift sensitivity to throttle increases at higher angles of attack, suggesting a strengthened coupling between propeller-induced flow and wing aerodynamics under elevated aerodynamic loading. Collectively, the structure of the identified model supports the central hypothesis that coordinated deployment of upward rotor tilt and downward elevon deflection enables efficient lift augmentation while preserving pitch controllability across the operating envelope, thereby supporting the proposed trim strategy for the tilt-rotor tailsitter configuration.

To visualize these effects, Fig. 7 presents the fitted response surface of lift force (F_{Z_A}) under fixed airspeed $V = 18$ m/s and throttle $T = 40\%$, evaluated at angles of attack $\alpha = 0°$, 5°, 10°, 15°, and 20°. Each subfigure overlays the model predictions with the corresponding measured data points. The lift surface derived from the fitted model matches the experimental measurements well across the full actuator space, demonstrating the local accuracy of the fitted model. Across all five cases, a consistent trend is observed that upward rotor tilt in combination with downward elevon deflection reaches the highest lift, confirming that the coordinated use of both elevons and rotor tilt can increase the maximum lift of a tailsitter compared to either actuation alone. In addition, increasing angle of attack from 0° to 20° steadily enhances the lift magnitude, reflecting the growing aerodynamic contribution from the wing at higher angle of attack. These results confirm that the model captures not only the effectiveness of individual actuators but also their interaction with flight condition.

To further quantify the agreement between the fitted model and the measurements, Fig. 8 presents two-dimensional cuts of the same fitted lift response surface at the tested rotor tilt angles $\delta_t = 0°$, 15.8°, 31.5°, and 47.3°. For each fixed rotor tilt angle, $F_{Z,A}$ is plotted against elevon deflection for $\alpha = 0°$, 5°, 10°, 15°, and 20°, under the same operating condition of $V = 18$ m/s and $T = 40\%$. The curves denote the fitted model predictions, while the markers denote the corresponding wind tunnel measurements. These cuts show that the fitted curves generally follow the measured data along representative slices of the actuator space. The model reproduces the main physical trends, including the increase in lift with angle of attack, the lift enhancement from downward elevon deflection, and the additional vertical force contribution from upward rotor tilt through thrust vectoring. Larger discrepancies are mainly observed for 20° angle of attack near large elevon deflections, where nonlinear control-surface effects and local flow separation are expected to become more pronounced. Overall, the agreement shown in both the global response surfaces and the two-dimensional cuts supports the use of the empirical model in the subsequent moment-equilibrium and maneuver-envelope analyses.

4. Enhanced lift with pitch moment equilibrium

Building on the empirical model developed from the static parameter sweep wind tunnel tests, the response surface analysis confirmed that upward rotor tilt and downward elevon deflection together contribute to increased lift. To further assess whether this lift-enhancing combination can also satisfy pitch moment equilibrium, a series of wind tunnel tests aimed at real-time moment trimming was carried out at an airspeed of 18 m/s. This airspeed was selected because it represents the high-speed forward-flight condition considered in the sharp-turn analysis and is consistent with the operating speed observed in prior outdoor flight experiments. It should be noted that the relative contributions of wing/elevon aerodynamics and propulsive forces are expected to vary with airspeed, due to changes in dynamic pressure and propeller inflow conditions. Therefore, the trim combinations obtained at 18 m/s should be interpreted as representative of this operating condition rather than as a complete speed-dependent trim map. A more comprehensive sensitivity study over multiple airspeeds remains an important direction for future work. For each angle of attack ($\alpha = 0°$, 5°, 10°, 15°, 20°, and 25°), the throttle was held constant at 45%, and the rotor tilt and elevon deflection were adjusted to reach a near-zero pitching moment, defined by $|M_y| < 0.02$ N·m. A closed-loop PID controller was employed to dynamically adjust the actuator settings using real-time feedback to satisfy the constraint above.

The pitching moment trimming process proceeded in three configurations to explore the role of different control strategies. First, to

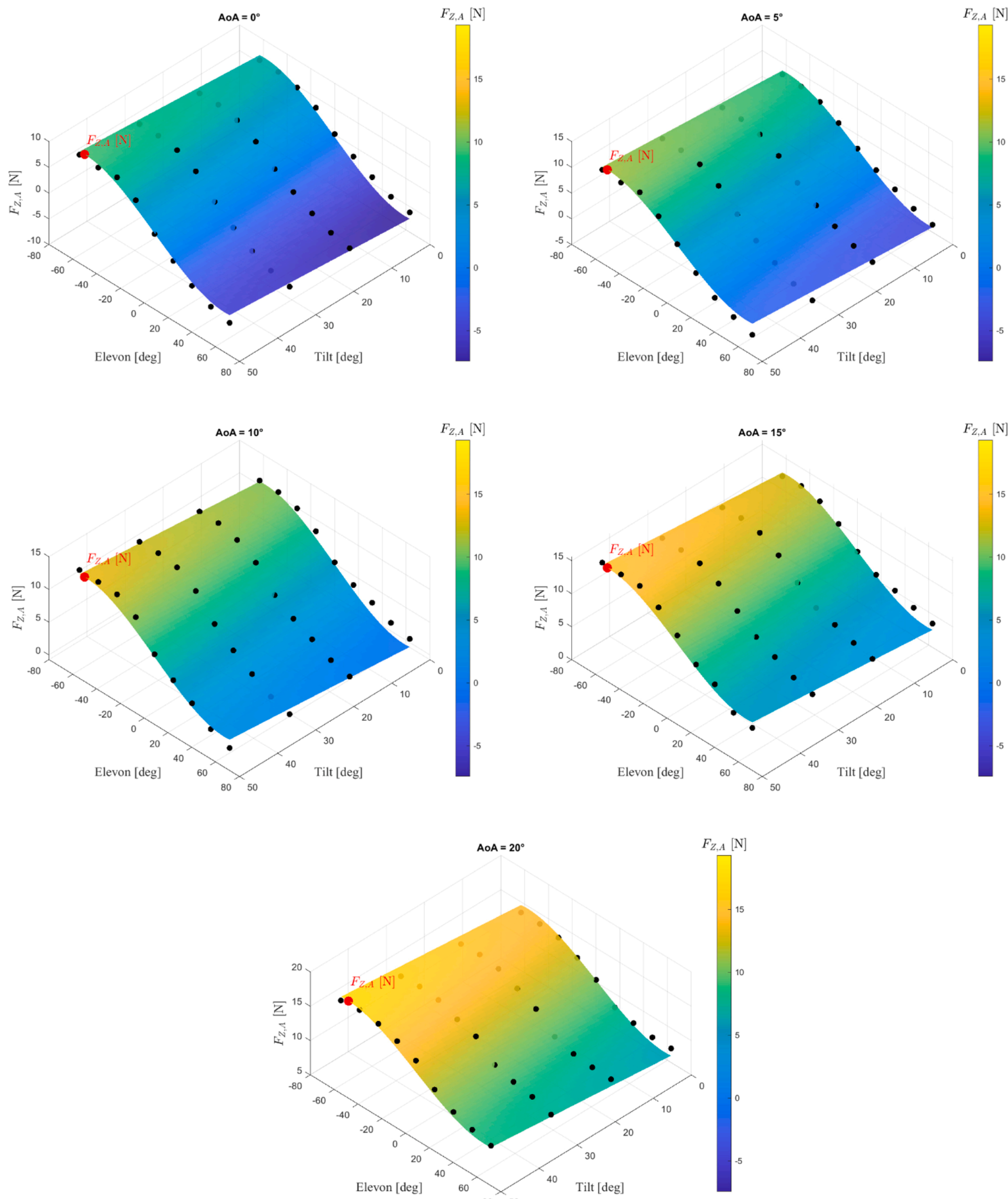

Fig. 7. Fitted response surfaces of lift force (F_z) under $V = 18$ m/s and $T = 40\%$, evaluated at $\alpha = 0°$, 5°, 10°, 15°, and 20°. Each subfigure shows the predicted lift across rotor tilt and elevon deflection, with overlaid experimental data points.

represent an E-tailsitter, the elevon was actuated while keeping the rotor tilt fixed at neutral ($\delta_t = 0°$), effectively using control surface deflection to offset the inherent pitch up or down moments from wing aerodynamics. Second, to characterize a TR-tailsitter, the reverse strategy was applied: elevon deflection was held at zero while the rotor tilt angle was varied to balance the pitch moment, leveraging the thrust vectoring effect of the tilted rotors. Finally, to analyze a TRE-tailsitter, a set of combined actuation tests were performed, where for each discrete rotor tilt angle ($\delta_t = 15.8°, 31.5°, 47.3°$), the elevon deflection was tuned dynamically to achieve moment balance. This last configuration directly tests the hypothesis that synergistic use of rotor tilt and elevon deflection can achieve pitch moment equilibrium with higher net lift than either control input alone.

Fig. 9 illustrates actuator combinations of elevon deflection and rotor tilt angle enabling pitch moment equilibrium for the three tailsitter categories, at 45% throttle, 18 m/s airspeed and different angles of attack. Across all configurations, the elevon deflection or the rotor tilt angle required for moment equilibrium increases with angle of attack. For the TRE-tailsitter, at low to moderate angles of attack, or at higher angles of attack with moderate rotor tilt, the elevons are able to counteract the pitch up moment induced by upward rotor tilt, achieving successful pitch moment trimming. However, when the angle of attack exceeds 15° and rotor tilt becomes large, the elevon rapidly saturates and no pitch moment equilibrium can be further achieved, which suggests that the wing stalls and flow separation occurs at the elevons in these cases. This limitation highlights the importance of actuator coordination and the trade-off between lift enhancement and moment controllability.

To further investigate the interaction between actuator inputs, lift generation, and pitching moment behavior, a series of contour plots was generated from the empirical model, as shown in Fig. 10. Each subplot depicts the predicted lift force $F_{Z,A}$ varying with rotor tilt and elevon deflection at a fixed throttle setting of 45% and airspeed of 18 m/s and different angles of attack. Superimposed on the lift contours are black dashed lines representing the pitching moment bounds $M_y = \pm 0.02$ N·m, which are consistent with the moment equilibrium threshold used in the pitching moment trim experiments.

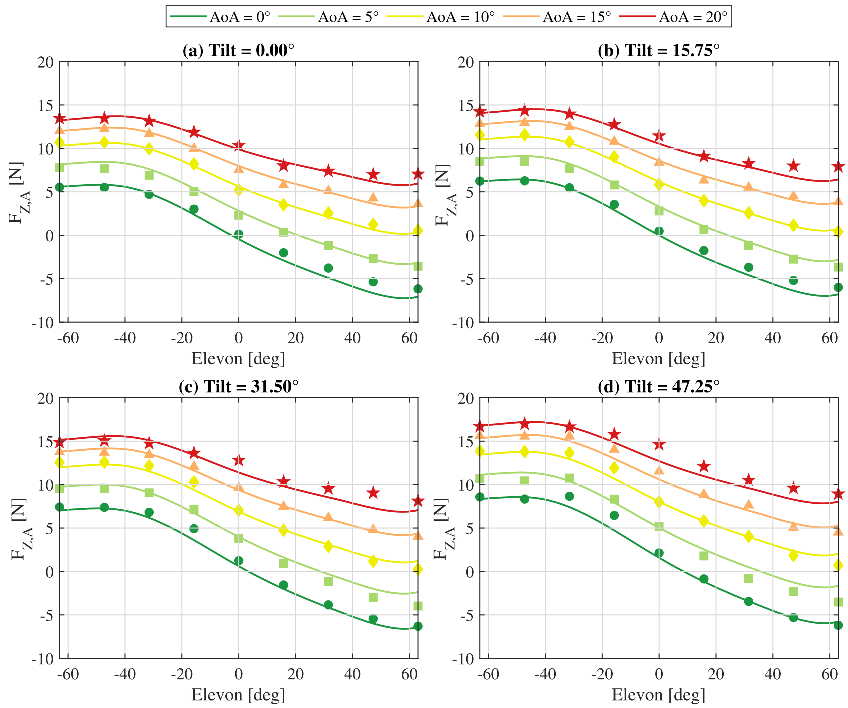

Fig. 8. Two-dimensional cuts of the fitted lift-force response surface at fixed rotor tilt angles under V = 18 m/s and T = 40%. Each subplot corresponds to a tested rotor tilt angle, δ_t = 0°, 15.8°, 31.5°, and 47.3°. The curves of different colors show the predicted variation of $F_{Z,A}$ with elevon deflection for α = 0°, 5°, 10°, 15°, and 20°, while the markers denote the corresponding wind-tunnel measurements.

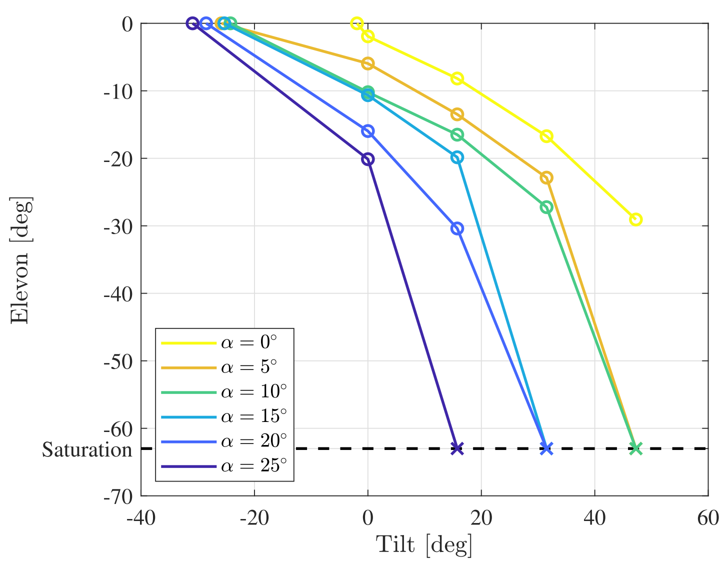

Fig. 9. Rotor tilt and elevon deflection combinations achieving pitch moment equilibrium ($|M_y|$ < 0.02 N·m) at various angles of attack under V = 18 m/s and 45% throttle. Open circles denote successful pitch moment trims; crosses indicate elevon saturation ($\delta_e = -63°$).

The plots reveal that pitch moment equilibrium is consistently achieved through coordinated actuator settings combining upward rotor tilt and downward elevon deflection. This actuator pairing not only satisfies moment balance but also yields substantially higher lift. As the angle of attack increases from 0° to 20°, the global lift magnitude rises as expected. However, the moment equilibrium contour progressively bends toward the elevon saturation boundary at higher angles of attack, indicating that moderate rotor tilt angles are sufficient to drive the elevon toward its actuation limit, consistent with the findings from pitching moment trim tests. This behavior suggests that while high angle of attack benefits lift generation, it imposes a rapidly increasing demand on the elevon's pitch down authority to counteract the pitch up moment brought by upward rotor tilt, thereby narrowing the available control margin.

Furthermore, the white stars in Fig. 10 denote actuator combinations satisfying pitch moment equilibrium measured during the above-mentioned pitch-trim wind tunnel experiments, corresponding to open circle points in Fig. 9. Notably, under the same flight condition of 45% throttle and 18m/s airspeed, these points fall within the $M_y = \pm 0.02$ contour bands predicted by the empirical model, thereby validating the model's accuracy in capturing the effect of actuator configurations on the aerodynamics of the TRE-tailsitter.

To achieve a sharp coordinated turn without losing speed, it is critical to ensure non-negative axial force. Fig. 11 illustrates the

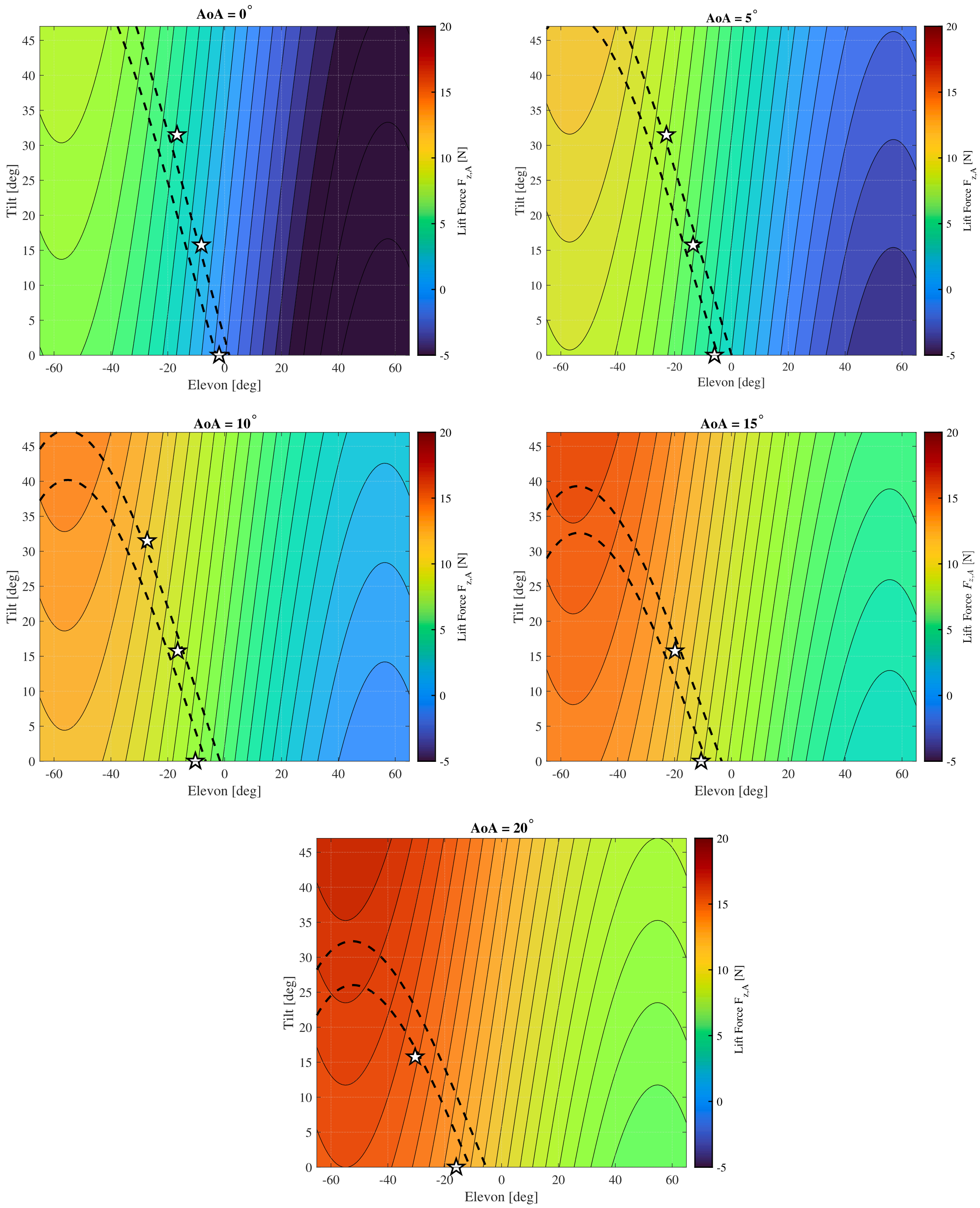

Fig. 10. Lift contour maps overlaid with allowable pitch moment equilibrium threshold ($|M_y| \leq 0.02$ N·m) at angles of attack $\alpha = 0°$, 5°, 10°, 15°, and 20°, under $V = 18$ m/s and 45% throttle. Each plot shows the predicted lift force ($F_{Z,A}$) as a function of rotor tilt and elevon deflection, based on the empirical model. The black dashed lines indicate trimmed moment threshold contours and stars represent the measurements from the pitching moment trim test under the same flight condition.

minimum throttle required to maintain positive axial force across various combinations of rotor tilt and elevon deflection, under fixed airspeed ($V = 18$ m/s) and different angles of attack. It should be noted that the minimum-throttle map is evaluated using the fitted empirical model over the full throttle-command range $T \in [0, 1]$, corresponding to 0% to 100% throttle. Since the static wind-tunnel measurements directly cover throttle settings only up to $T = 0.45$, regions requiring $T > 0.45$ should be interpreted as extended-throttle-command model estimates. A consistent trend is observed where higher angles of attack require greater throttle input, reflecting the increased aerodynamic drag associated with high angle of attack. A general monotonic trend is observed in which the minimum throttle requirement increases with rotor tilt, as a larger fraction of thrust is progressively redirected from the axial to the vertical direction. However, the sensitivity of required throttle to rotor tilt is not uniform across the entire range. At moderate tilt angles, approximately 0°–25°, the throttle contours become noticeably flatter, suggesting a regime in which the adverse effect of thrust projection loss is partially mitigated by favorable aerodynamic interactions between the propeller slipstream and the wing, potentially improving boundary-layer attachment and reducing effective drag. Beyond this region, the throttle demand rises rapidly with further increases in rotor tilt, reflecting the dominance of geometric projection loss of thrust in the axial direction.

The influence of elevon deflection on the axial-force balance becomes particularly pronounced at high angles of attack. As shown in Fig. 11, at low angles of attack, the minimum throttle requirement exhibits relatively weak sensitivity to elevon deflection. However, as the angle of attack increases, a clear asymmetry emerges between upward and downward deflections. In the high angle of attack regime, downward elevon deflection leads to a rapidly increasing throttle demand. For excessively large downward deflections, the required throttle approaches the saturation boundary imposed by the propulsion system. This behavior reflects the combined effect of increased profile drag, enhanced downwash curvature, and deterioration of flow attachment at large negative deflections. In contrast, configurations with upward elevon deflection remain within the achievable throttle envelope even at high angles of attack. Overall, the results reveal that at high angles of attack, downward elevon deflection represents a critical limiting factor for axial-force sustainability, whereas upward deflections retain a greater operational margin in terms of propulsion demand.

5. Minimum radius for high-speed sharp turn

In a high-speed coordinated turn, the aircraft must generate a sufficient lift force in order to provide the centripetal force required to sustain the maneuver, while simultaneously maintaining a stable pitch attitude. To keep consistent with the wind tunnel testing conditions where dynamic pitching was absent, we assume that the rotational pitch rate q has no effect on aerodynamic forces and moments. Accordingly, transient aerodynamic effects and actuator response dynamics during maneuver execution are not modeled in the present analysis. To identify actuation strategies that enable sharp turning, a parametric search was performed using the empirical aerodynamic models derived in Section 3.3 over the actuator space spanned by rotor tilt and elevon deflection.

The actuator search was constrained by the tested actuator ranges used to construct the empirical model. Specifically, the rotor-tilt range was restricted to $\delta_t \in [0°, 47.3°]$ and the elevon deflection range was $\delta_e \in [-63°, 63°]$. Although the same type of servos were used for the rotor-tilt and elevon mechanisms with a nominal range of $[-63°, 63°]$, large positive rotor-tilt angles close to the full servo range imposed excessive loading on the tilt servo during the wind tunnel tests at $V = 18$ m/s. Therefore, the rotor-tilt range used in the analysis was limited to the experimentally tested range. The throttle command was allowed to vary over the full command range $T \in [0, 1]$, whereas the static wind-tunnel measurements used for model fitting directly cover throttle settings only up to $T = 0.45$. Therefore, predictions for $T > 0.45$ should be interpreted as extended-throttle-command model estimates. Thus, actuator position limits are included in the parametric search, but actuator dynamics such as rate limits and response delays are not considered. The analysis of the minimum radius of a high-speed sharp turn focused on a representative forward flight condition at an airspeed of 18 m/s within the angle of attack range of 0° to 20°. For each candidate combination (δ_t, δ_e), an inner search was conducted over angle of attack α and throttle setting T to identify feasible operating points satisfying both the pitching moment equilibrium condition $|M_y| \leq 0.02$ N·m and the axial-force constraint $|F_{X,A}| \leq 0.1$ N. This effectively simulates the constraints of a banked turn, where both pitch moment stability and lift generation must be ensured while maintaining the forward speed. The resulting minimum turning radius should be interpreted as a quasi-static performance bound under equilibrium constraints rather than as a complete dynamic trajectory prediction.

Among all angle of attack and throttle pairs (α, T) at a given actuator configuration, the maximum achievable lift was extracted and defined as the local maximum lift associated with that (δ_t, δ_e) point. By repeating this procedure throughout the (δ_t, δ_e) grid, a contour map of local maximum lift over the actuator space was constructed, as shown in Fig. 12. It is important to note that each point on this map corresponds to a distinct combination of optimal angle of attack and throttle setting, rather than a common operating condition shared across the figure.

The red dot markers in Fig. 12 highlight two groups of representative local optima, which compares the locally optimal lift both across rotor tilt at fixed elevon deflection and across elevon deflection at fixed rotor tilt. For each actuator setting (δ_t, δ_e) marked by a red dot, the corresponding optimal angle of attack, throttle command, and predicted lift level (α, T, F_z) are explicitly annotated in the figure, emphasizing that every point on the contour map is associated with its own optimal operating condition in (α, T) rather than a single global flight condition. The global maximum lift, obtained by comparing all local optima across the actuator space, is denoted by the red hexagram in Fig. 12. The global maximum lift predicted by the extended-command search occurs at $\alpha = 18°$, $T = 1.00$, $\delta_t = 19°$, and $\delta_e = -63°$, yielding $F_{Z,A} = 20.35$ N, corresponding to approximately 4.25 times the vehicle weight ($m = 0.489$ kg). Since the throttle command at this operating point is above the directly tested static throttle levels, the predicted lift value should be interpreted as an extrapolated estimate from the fitted empirical model. It nevertheless indicates that the vehicle is capable of generating sufficiently large lift forces to sustain aggressive coordinated turns under the imposed pitch moment and axial force equilibrium constraints.

Building on the identified maximum lift and its corresponding actuator configuration, we proceed to compute the minimum turning radius for a coordinated turn. By projecting the gravity defined in the East-North-Up inertial frame and the aerodynamic force defined in the aerodynamic frame (as defined in Fig. 4) onto the trajectory frame, the following expressions are obtained:

$$F_G = \begin{bmatrix} \cos\gamma & 0 & -\sin\gamma \\ 0 & 1 & 0 \\ \sin\gamma & 0 & \cos\gamma \end{bmatrix} \begin{bmatrix} \cos\xi & \sin\xi & 0 \\ -\sin\xi & \cos\xi & 0 \\ 0 & 0 & 1 \end{bmatrix} \begin{bmatrix} 0 \\ 0 \\ -mg \end{bmatrix}, \tag{9}$$

$$F_A = \begin{bmatrix} 1 & 0 & 0 \\ 0 & \cos\mu & \sin\mu \\ 0 & -\sin\mu & \cos\mu \end{bmatrix} \begin{bmatrix} -D \\ Y \\ L \end{bmatrix}, \tag{10}$$

where γ is the flight path angle, ξ is the aerodynamic heading angle, and μ is the aerodynamic bank angle, and D, Y, and L denote drag, side force, and lift, respectively. Consequently, the resultant force acting on the drone in the trajectory frame is given by

$$F_T = F_G + F_A = \begin{bmatrix} mg\sin\gamma - D \\ Y\cos\mu + L\sin\mu \\ -mg\cos\gamma - Y\sin\mu + L\cos\mu \end{bmatrix}. \tag{11}$$

Here, it is assumed that the aircraft is in a level flight phase, with a flight-path angle of zero, i.e., $\gamma = 0$. Furthermore, for symmetric aircraft, e.g. the proposed TRE-tailsitter, under normal flight conditions without sideslip, the aerodynamic side force Y is considered negligible. Therefore, the forces acting on the aircraft in the trajectory frame can be simplified as

$$F_T = \begin{bmatrix} -D \\ L\sin\mu \\ -mg + L\cos\mu \end{bmatrix}. \tag{12}$$

The force along the Y-axis of the trajectory frame provides the centripetal force required for turning, and the force along the Z-axis is zero due to the assumption of level flight. Accordingly, it follows that $\cos\mu = \frac{mg}{L}$, and thus $|\sin\mu| = \sqrt{1 - \frac{m^2g^2}{L^2}}$. As a result, the turning radius can be calculated by the following formula:

$$R = \frac{mV^2}{|L\sin\mu|} = \frac{mV^2}{\sqrt{L^2 - m^2g^2}}. \tag{13}$$

Given the predicted maximum lift of 20.351 N obtained under pitch moment equilibrium and near-zero axial force at the extended throttle command of 100%, the theoretical minimum turning radius for a 0.489 kg TRE-tailsitter during an 18 m/s coordinated turn is calculated by Eq. (13) as 8.01 m.

To evaluate the effect of empirical-model fitting errors on the predicted minimum turning radius, the sharp-turn search was repeated using RMSE-based conservative perturbations. The lift prediction was reduced before computing the turning radius, while the axial-force and

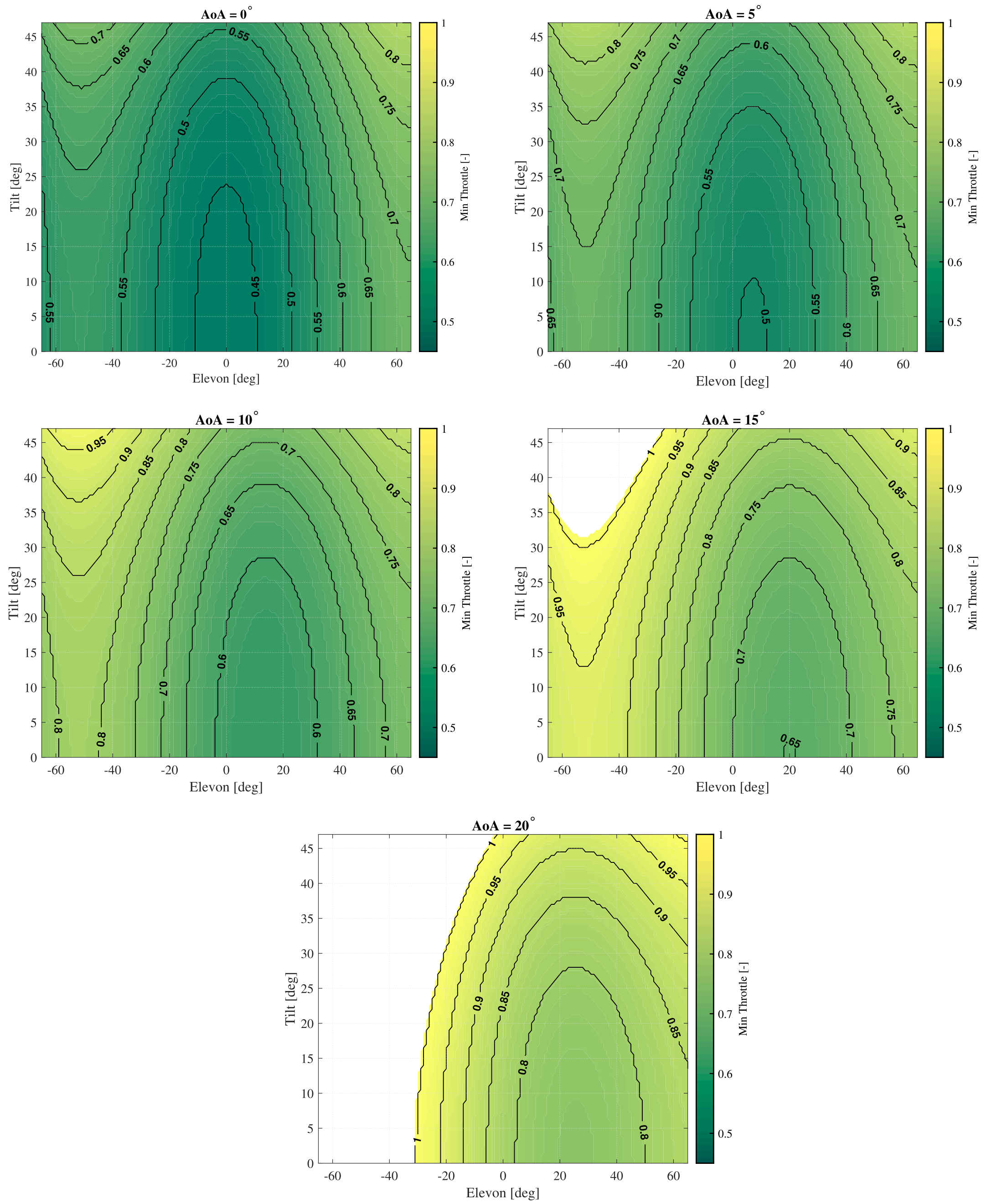

Fig. 11. Contour plots for the minimum throttle required to sustain positive axial force across rotor tilt and elevon deflection combinations at various angles of attack ($\alpha = 0° \sim 20°$), under $V = 18$ m/s.

pitching-moment constraints were tightened to reflect fitting-error margins in the feasibility conditions. For a perturbation level k, expressed as a fraction of the corresponding RMSE, the modified search conditions are defined as

$$\begin{aligned} &F_{Z,A}^{\text{eff}} = F_{Z,A}^{\text{pred}} - k\,\text{RMSE}_{F_Z}, \\ &\left|F_{X,A}^{\text{pred}}\right| + k\,\text{RMSE}_{F_X} \le 0.1\ \text{N}, \\ &\left|M_y^{\text{pred}}\right| + k\,\text{RMSE}_{M_y} \le 0.02\ \text{N}\cdot\text{m}, \end{aligned} \tag{14}$$

where $F_{Z,A}^{\text{pred}}$, $F_{X,A}^{\text{pred}}$, and M_y^{pred} denote the empirical-model predictions and $F_{Z,A}^{\text{eff}}$ is the conservative lift estimate used in the turning-radius calculation after accounting for the RMSE-based perturbation. Since the parametric search for the sharp turn maneuver uses strict bounds on $F_{X,A}$ and M_y, applying their full RMSE values directly as additional constraint offsets would be overly conservative and would eliminate most or all feasible solutions. Fractional RMSE values are therefore used to examine how the optimum changes as the axial-force and pitching-moment requirements are progressively tightened.

The results are summarized in Table 3. Among the tested perturbations, the minimum-radius estimate shows the highest sensitivity to the lift-force model. Reducing $F_{Z,A}$ by 0.5RMSE_{F_Z} and 1.0RMSE_{F_Z} increases $R_{\min}$ from the nominal 8.011 m to 8.139 m and 8.271 m, corresponding to increases of 1.60% and 3.25%, respectively. Compared with the lift perturbation, the constraint-based perturbations mainly affect the feasible set and lead to smaller changes in $R_{\min}$. With an additional 0.2RMSE_{F_X} offset in the axial-force constraint, the optimum shifts from $(\alpha, T, \delta_t, \delta_e) = (18°, 1.00, 19.0°, -63.0°)$ to $(17°, 1.00, 21.5°, -60.5°)$, while the predicted radius increases by only 0.87%. For the pitching-moment constraint, applying a 0.2RMSE_{M_y} offset does not change the optimum,

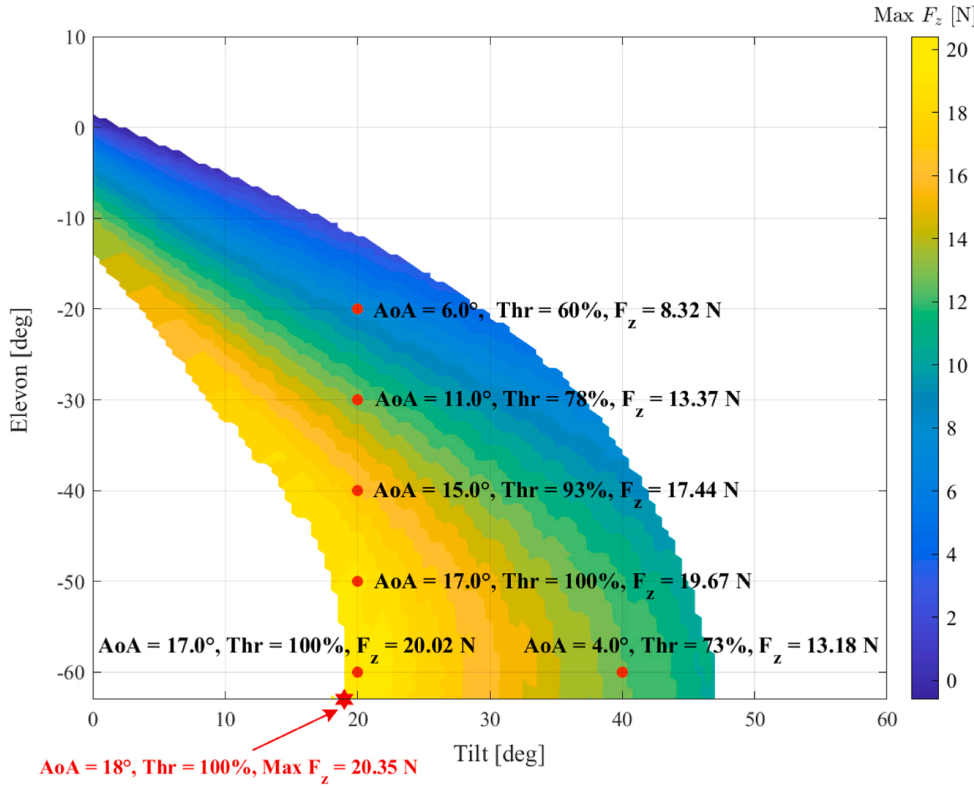

Fig. 12. Maximum lift force ($F_{Z,A}$) achievable across rotor tilt and elevon deflection combinations at 18 m/s airspeed, while satisfying $|F_{X,A}| < 0.1$ N and $|M_y| < 0.02$ N·m. The red hexagram denotes the global maximum lift point and the red dots represent local maximum lift points. (For interpretation of the references to colour in this figure legend, the reader is referred to the web version of this article.)

Table 3
Sensitivity of the predicted minimum turning radius to empirical-model fitting errors.

Case	$R_{\min}$ [m]	ΔR [%]	α [deg]	T	(δ_t, δ_e) [deg]
Nominal	8.011	0.00	18	1.00	(19.0, −63.0)
$F_{Z,A}$ − 0.5RMSE	8.139	1.60	18	1.00	(19.0, −63.0)
$F_{Z,A}$ − 1.0RMSE	8.271	3.25	18	1.00	(19.0, −63.0)
$F_{X,A}$ robust 0.2RMSE	8.081	0.87	17	1.00	(21.5, −60.5)
M_y robust 0.2RMSE	8.011	0.00	18	1.00	(19.0, −63.0)
Combined	8.371	4.50	17	1.00	(21.0, −60.0)

since the nominal solution remains feasible under the stricter moment bound. In the combined case, where the lift prediction is reduced by one full RMSE and both feasibility constraints are tightened by 0.2 times their corresponding RMSE values, the predicted radius increases to 8.371 m, corresponding to a 4.50% increase. Overall, the sensitivity analysis indicates that the minimum-radius estimate is mainly governed by the lift-force prediction, but remains within approximately 5% of the nominal value under the tested fitting-error perturbations.

To enable a baseline comparison against a conventional fixed-rotor E-tailsitter with an identical airframe but without thrust-vectoring authority, the same parametric search was repeated while confining the rotor tilt to 0°. Under the same equilibrium and near-zero axial-force constraints ($|F_{X,A}| < 0.1$ N and $|M_y| < 0.02$ N·m), the maximum achievable lift decreases to 14.319 N, yielding a theoretical minimum turn radius of 11.74 m. These results indicate that the coordinated use of rotor tilt and elevon deflection for a TRE-tailsitter increases the maximum lift during a coordinated turn by 42.1% and reduces the theoretical minimum turn radius by 31.8% compared to the conventional fixed-rotor E-tailsitter configuration. It should also be emphasized that this sensitivity analysis evaluates the effect of empirical-model fitting errors within the extended-command search. It does not remove the throttle extrapolation associated with the $T = 1.00$ optimum, and the absolute value of the minimum radius should therefore still be interpreted as an extrapolated theoretical bound.

6. Conclusion

This study experimentally quantifies the coupled effects of rotor tilt and elevon deflection on a tilt-rotor tailsitter through extensive wind-tunnel measurements and empirical modeling. The results show that, within the tested positive-AoA forward-flight wind-tunnel envelope, coordinated use of upward rotor tilt and downward elevon deflection enables substantial lift augmentation while maintaining pitch moment equilibrium. However, this benefit is constrained by elevon saturation at high angles of attack, as increasing aerodynamic loading drives the required pitch down authority beyond actuator limits. This reveals a fundamental tradeoff between lift maximization and pitch controllability that governs the feasible trim envelope of the tilt-rotor tailsitter under the tested conditions.

By embedding the derived aerodynamic models into a parametric equilibrium-constrained performance analysis, the study provides insight into actuator coordination for agile maneuvers. At an operating point characterized by a high angle of attack, full throttle, moderate upward rotor tilt, and maximum downward elevon deflection, the extended-throttle-command analysis predicts an extrapolated theoretical minimum turning radius of 8.01 m at 18 m/s, representing a 31.8% reduction compared to the 11.74 m baseline of a conventional fixed-rotor tailsitter with elevons under the same analysis assumptions. Since this optimum occurs at full throttle command of 100%, beyond the maximum static throttle level directly tested in the wind-tunnel matrix, this value should be interpreted as an extrapolated performance bound predicted by the wind-tunnel-derived empirical model under the extended throttle-command range, rather than as a fully experimentally validated flight performance prediction. Nevertheless, these results demonstrate that aggressive turning performance is realized not through extreme reliance on a single actuator, but through balanced allocation between thrust vectoring and aerodynamic control surfaces. The findings provide experimental evidence for actuator synergy in hybrid VTOL aircraft and offer a practical framework for performance-oriented control allocation and envelope exploitation in tilt-rotor tailsitter designs.

Future work will extend the present findings through high-throttle wind-tunnel measurements and outdoor flight experiments, focusing on high-speed turning maneuvers to validate the predicted optimal configurations under realistic conditions. These tests will assess not only aerodynamic model fidelity but also the impact of actuator dynamics, control bandwidth, and environmental uncertainty on achievable maneuver performance.

CRediT authorship contribution statement

Ziqing Ma: Writing – original draft, Methodology, Formal analysis; **Ewoud J. J. Smeur:** Writing – review & editing, Supervision, Conceptualization; **Guido C. H. E. de Croon:** Writing – review & editing, Supervision.

Declaration of competing interest

The authors declare that they have no known competing financial interests or personal relationships that could have appeared to influence the work reported in this paper.

Acknowledgement

The authors would like to thank Liming Zheng and Baihui Chen for their help with the wind tunnel test setup.

Data availability

Research Dataset Link Provided

References

[1] J. Zhong, W. Chen, Transition characteristics for a small tail-sitter unmanned aerial vehicle, Chin. J. Aeronaut. 34 (10) (2021) 220–236.
[2] E.A. Islas-Narvaez, J.F. Ituna-Yudonago, L.E. Ramos-Velasco, M.A. Vega-Navarrete, O. Garcia-Salazar, Design and determination of aerodynamic coefficients of a tail-Sitter aircraft by means of CFD numerical simulation, Machines 11 (17) (2023) 1–24.
[3] K. Anuar, W. Fatra, A. Asral, N. Nazaruddin, M. Taslim, Preliminary design of tail-sitter UAVs, in: 3Rd Conference on Innovation in Technology and Engineering Science (CITES), Vol. 2891, AIP Publishing, 2022, pp. 1–11.
[4] E.A. Tal, S. Karaman, Global trajectory-tracking control for a tailsitter flying wing in agile uncoordinated flight, in: AIAA Aviation 2021 Forum, (no. 3214), AIAA, 2021, pp. 1–20.
[5] G.H. Lovell-Prescod, Z. Ma, E.J.J. Smeur, Attitude control of a tilt-rotor tailsitter micro air vehicle using incremental control, in: 2023 International Conference on Unmanned Aircraft Systems (ICUAS), IEEE, 2023, pp. 842–849.
[6] Z. Ma, E.J.J. Smeur, G.C. H.E. De Croon, Design and control of a tilt-Rotor tailsitter aircraft with pivoting VTOL capability, IEEE Robot. Autom. Lett. 10 (6) (2025) 5911–5918.
[7] R. Chiappinelli, M. Nahon, Modeling and control of a tailsitter UAV, in: 2018 International Conference on Unmanned Aircraft Systems (ICUAS), IEEE, 2018, pp. 400–409.
[8] E. Tal, S. Karaman, Global incremental flight control for agile maneuvering of a tailsitter flying wing, J. Guid. Control Dyn. 45 (12) (2022) 2332–2349.
[9] P. Aref, M. Ghoreyshi, A. Jirasek, M.J. Satchell, K. Bergeron, Computational study of propeller–wing aerodynamic interaction, Aerospace 5 (3) (2018) 79.
[10] R.H. Stone, Aerodynamic modeling of the wing-propeller interaction for a tail-sitter unmanned air vehicle, J. Aircr. 45 (1) (2008) 198–210.
[11] A. Zanotti, A. Savino, M. Palazzi, M. Tugnoli, V. Muscarello, Assessment of a mid-fidelity numerical approach for the investigation of tiltrotor aerodynamics, Appl. Sci. 11 (8) (2021) 3385.
[12] L. Ye, Y. Zhang, S. Yang, X. Zhu, J. Dong, Numerical simulation of aerodynamic interaction for a tilt rotor aircraft in helicopter mode, Chin. J. Aeronaut. 29 (4) (2016) 843–854.
[13] S. Srivathsan, J. Rauleder, Experimental wind tunnel investigation on propeller-wing interactional aerodynamics, in: AIAA SCITECH 2023 Forum, (no. 1752), 2023.
[14] H. Jois, A.S. Hong, P.J. Ansell, High-lift aerodynamics of integrated distributed propulsion systems with thrust vectoring, J. Aircr. 61 (6) (2024) 1686–1699.
[15] Z. Ma, E.J.J. Smeur, Wind tunnel test dataset of a tilt-rotor tailsitter focusing on wing-propeller interaction, 4TU.ResearchData (2025). dataset. https://doi.org/10.4121/8b78a204-e41e-4ec3-ae5d-dbb8df7f8922.
[16] H.J. Alons, OJF External balance documentation, Natl. Lucht Ruimtevaartlaboratorium (2008).
[17] Z. Ma, E.J.J. Smeur, G.C. H.E. de Croon, Wind tunnel tests of a wing at all angles of attack, Int. J. Micro Air Veh. 14 (2022) 1–11.
[18] R. Tibshirani, Regression shrinkage and selection via the lasso, J. R. Stat. Soc. B: Stat. Methodol. 58 (1) (1996) 267–288.